Engineering salt-rejecting solar evaporator from naturally hierarchical tree root for sufficient clean water production

Qin, Jinli; Xu, Wenyang; Li, Yongzheng; Wang, Xiaodi; Wu, Ruijie; Fu, Yingjuan; Qin, Menghua; Zhang, Yongchao; Xu, Chunlin

Published in:
Industrial Crops and Products

DOI:
10.1016/j.indcrop.2023.116507

Published: 01/06/2023

Document Version
Final published version

Document License
CC BY

Industrial Crops & Products 196 (2023) 116507

Contents lists available at ScienceDirect

Industrial Crops & Products

journal homepage: www.elsevier.com/locate/indcrop

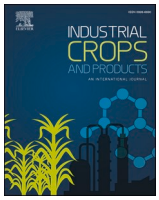

Engineering salt-rejecting solar evaporator from naturally hierarchical tree root for sufficient clean water production

Jinli Qin [a], Wenyang Xu [c], Yongzheng Li [a], Xiaodi Wang [b], Ruijie Wu [c], Yingjuan Fu [a], Menghua Qin [b], Yongchao Zhang [a,*], Chunlin Xu [c,*]

[a] State Key Laboratory of Biobased Material and Green Papermaking, Qilu University of Technology, Shandong Academy of Sciences, Jinan 250353, Shandong, China
[b] Organic Chemistry Laboratory, Taishan University, Taian 271021, China
[c] Laboratory of Natural Materials Technology, Åbo Akademi University, Turku Fi-20500, Finland

ARTICLE INFO

Keywords:
Tree root
Natural millimeter-sized channels
Mountain-shaped Fe_3O_4 inner surface
Anti-salt-accumulation
Solar desalination

ABSTRACT

Solar desalination has been recognized as one of the most promising technologies for solving current freshwater scarcity. However, enhancement of the photothermal conversion efficiency and prohibiting salt crystallization on the top light-absorbing surface are the two major critical challenges for developing highly-efficient and stable solar evaporators. Here, we have discovered that tree roots, often as processing waste when utilizing woods, can serve as a high-efficient solar evaporation device for continuous desalination. The naturally occurring hierarchical structure of tree roots possesses multilevel longitudinal channels from micrometer to millimeter-scale and interconnected porous microstructures, which allows excellent water transport and multidirectional salt exchange, exhibiting a superior anti-salt-accumulation capability even in 21% brine. Together with a mountain-shaped hydrophobic absorber surface obtained from the *in situ* synthesized Fe_3O_4 nanoparticles, the designed tree root-based solar evaporator demonstrates an evaporation rate of 1.64 kg m^{-2} h^{-1} and ultra-high conversion efficiency of 96% at 1 solar irradiation, rendering it as one of the best performing wood-based solar evaporators. Furthermore, such a high-efficacy, techno-economic and long-term stable seawater desalination platform provided by the architectures of multi-level channel-array in tree root will inspire material scientists and engineers to tailor structurally similar materials from building blocks of broader selections.

1. Introduction

Freshwater scarcity is an urgent challenge needed to overcome due to the growing world population, active civilization, and deteriorating environment (Elimelech and Phillip William, 2011; Kumar et al., 2021; Kummu et al., 2016). Solar vapor generation utilizes photothermal materials to convert sustainable solar energy into thermal energy for generating steam from salt water and other contaminants (Wang et al., 2021). The techno-economic, high-efficacy, and sustainable features of solar-thermal desalination device greatly satisfies the alleviation of water scarcity (Tao et al., 2018; Zhou et al., 2019). A typical configuration of solar evaporator design with top surface of the photothermal layer for solar absorbers and bottom layer of the sponge-like supporting substrates for water transfer (Zhao et al., 2020; Zhu et al., 2019). Tremendous research focused on developing sustainable solar desalination devices and increasing their efficiency, while several critical challenges remain (Bian et al., 2021; Chen et al., 2019; Xu et al., 2021). The increased salinity with heating-induced evaporation causes the increasing formation of salt crystals with the concentrated brine on the evaporative surface, drastically reducing solar absorption and photothermal conversation (Djellabi et al., 2022; Li et al., 2019; Wang et al., 2020; Xu et al., 2020; Zang et al., 2021). Furthermore, this will block water transportation path, resulting in diminished efficiency and even interrupting evaporation.

The solar evaporators with highly salt-resistant property by using a hydrophobic interface have been attempted (Li et al., 2021; Li et al., 2020; Storer et al., 2020; Zhang et al., 2020). However, the evaporation efficiency of currently available solar desalination systems for stable water desalination is relatively low, especially for the high salinity brine, due to the heat loss caused by material and the reduction of light absorbance. Meanwhile, the complex processes of synthetic top/bottom materials and/or costly materials limits their industrial production and large-scale application (Han et al., 2021; Shi et al., 2022; Tian et al., 2020; Wei et al., 2021; Zhu et al., 2018). The used synthetic polymers in

* Corresponding authors.
E-mail addresses: yongchaoaaaa@163.com (Y. Zhang), cxu@abo.fi (C. Xu).

https://doi.org/10.1016/j.indcrop.2023.116507
Received 27 November 2022; Received in revised form 28 January 2023; Accepted 26 February 2023
Available online 1 March 2023

solar evaporators have raised significant environmental concerns because of the difficulty of disposal issues such as degradability and leaching (Jiang et al., 2017; Li et al., 2020). Therefore, it is imperative to develop cost-effective and sustainable solar evaporator, simultaneously achieving long-term stability and high efficiency of evaporation in the brine with a wide concentration range.

Wood trunks have been utilized to produce solar desalination devices with their intrinsically aligned vertical porous structure (Cao et al., 2021; Jia et al., 2017; Li et al., 2018; Wang et al., 2019; Xue et al., 2017; Zhu et al., 2018). Structure engineering of wood with drilling millimeter-scale deep holes in the material matrix was found to overcome the salt accumulation-related issues (Kuang et al., 2019; Sharshir et al., 2022). Unique wood species with large-diameter vessels or tracheids could be directly employed to fabricate salt-accumulation-free solar evaporator (Chen et al., 2017; He et al., 2019). Compared with wood trunk (Fig. 1a), the conduit diameter and hydraulic conductivity of root were the largest and highest than other parts of the tree (Hafner et al., 2020; McElrone et al., 2004). The channels on the root section with large channel up to 260 μm in diameter are visible (Fig. 1b), compared with dense trunk wood (elm wood) with channel diameter of vessels ranging from 3 μm to 30 μm (Fig. 1b). The low bending large-diameter channels and narrow channels communicate with each other through pits in the wall (Fig. 1c). The large channel derived from the conduit of tree root has a higher water flux than other small-sized channels (McElrone et al., 2004). Those intrinsic hierarchical structures render an in-plane salt concentration gradient in the presence of low salt concentration in large channels and relative high salinity in the small-sized channels under the same condition. The salinity gradient furthermore benefits a spontaneous salt exchange and receives self-regenerating (Kuang et al., 2019). In addition, the high hydraulic conductivities allow rapid delivery of water compared with wood trunk (Hafner et al., 2020; McElrone et al., 2004). Therefore, nature-created tree root offers an ideal substrate to be directly converting to solar evaporators having superior salt resistance.

Herein, inspired by the unique multi-level channel microstructure and fast water transport capability of tree roots, for the first time, we designed a natural root-based solar evaporator with anti-salt-accumulation property for sustainable desalination. Moreover, to achieve high evaporation efficiency, two-step modifications were conducted: (i) enforcing the slight delignification process of tree root to improve the substrate of hydrophilicity and water transportation capability; (ii) *in situ* synthesis of Fe_3O_4 nanoparticles on the surface of root substrate to form a nanostructured mountain-shaped absorber surface in order to enhance light absorption. The high specific surface area and surface roughness of above-mentioned solar vapor generation significantly reduces the diffuse scattering of light, and greatly convert solar irradiation into thermal energy. The vapor generators remarked a new record of water evaporation rate of ≈ 1.64 kg m^{-2} h^{-1} and super-high conversion efficiency of 96% under 1 sun irradiation in seawater conditions, rendering it as the best performing wood-based photothermal material. Upon intrinsic hierarchical design of micro-structure and absorber, the fabricated root-based solar also exhibited outstanding evaporation efficiency and stability in high salinity (21%) brine desalination.

2. Material and methods

2.1. Materials

Elm tree, root, were obtained from north of China (Shandong Province); 30% H_2O_2 solution, Trisodium citrate dihydrate, $FeCl_2$•4 H_2O, $FeCl_3$•6 H_2O, sodium chloride, Barium chloride, sodium hydroxide, and ammonia were all provided by Sinopharm Group.

2.2. Fabrication of the tree roots-solar vapor generators (FPTRW)

Briefly, the preparation process is divided into two steps. The first step is the process of partial lignin removal: tree roots were cut into round wood pieces with a thickness of 3 mm, put into a 500 ml beaker, to which 400 ml of preconfigured 12% sodium hydroxide solution was added, heated it to 95 °C, and steamed under stirring for 3 h and then the wood pieces were removed. Finally, the wood chips were washed several times in 90 °C water to near neutral to remove sodium hydroxide and lignin from the surface of the chips. The second step was typical *in situ* synthesis process to load Fe_3O_4 nanoparticles onto the pretreated wood chips. Firstly, ferric chloride hexahydrate (ferric trichloride, 8.6763 g) and ferrous chloride tetrahydrate (ferrous chloride, 3.9840 g) were dissolved in deionized water (100 ml) and the wood chips were

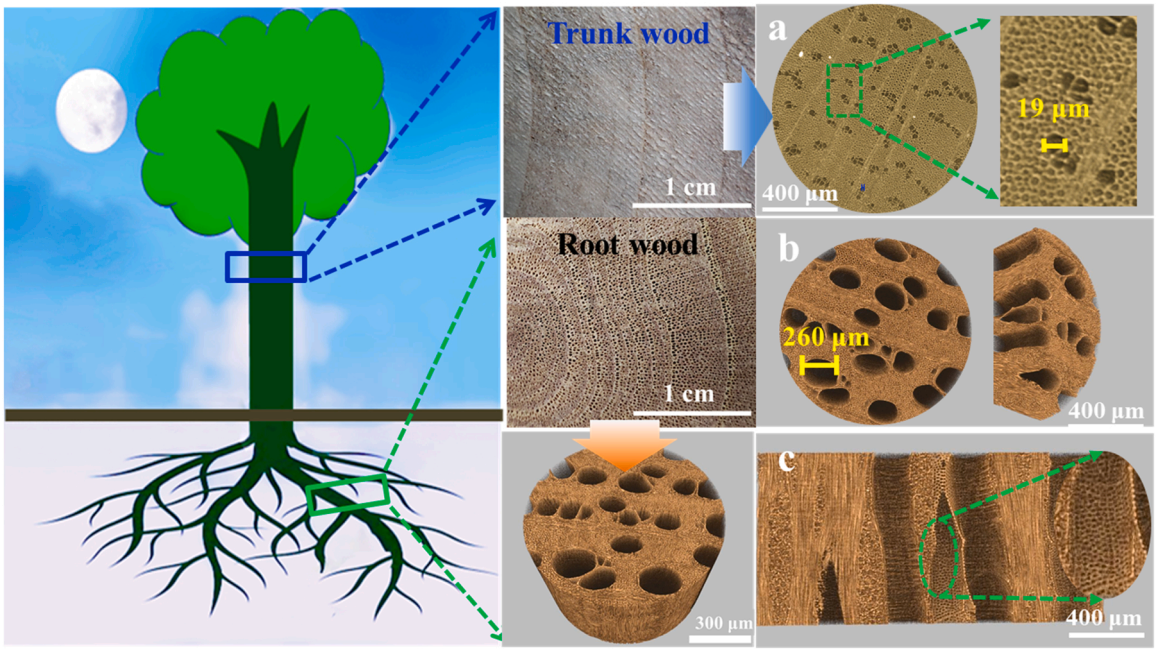

Fig. 1. Photographs and microscopic images showing the integrated structure and multi-level channel-array of trunks and roots from the elm tree by micro-CT.

placed in it. Then ammonia (ammonium hydroxide, 100 ml) was added and heated in a water bath at 70 °C for 30 min. After that, trisodium citrate dihydrate (trisodium citrate, 10.2224 g) was added and heated in a water bath at 40 °C for 120 min. In this process, the generated Fe_3O_4 nanoparticles were loaded onto the pretreated tree root pieces to obtain FPTRW. Finally, the FPTRW were washed to neutral in water at 40 °C, then dried, sealed, and refrigerated for subsequent experiments.

2.3. Solar desalination experiments

The solar desalination experiments were carried out at room temperature (humidity ~32%). Solar-driven water evaporation simulations were performed using a solar simulator (CEL-HXF300-T3, CEAULIGHT, Beijing, China). The temperature of evaporator top surface was recorded by an infrared thermal imager and the weight change of the bottle was monitored in real-time by an analytical balance (0.1 mg resolution). NaCl solution was used to simulate seawater. The energy efficiency (η) is obtained by the following formula : .

$\eta = m\ h_{lv}/C_{opt}\ P_0$ (1).

in which m is the mass flux, hlv is the enthalpy of phase change (liquid to vapor), P_0 is the solar irradiation power of one sun (1 kW m^{-2}).

2.4. Characterizations

The morphology of the samples was characterized by scanning electron microscopy (SEM, JSM-7500 F) at the accelerating voltage of 10 kV and a SkyScan 2211 micro-CT (Bruker, Knotich, Belgium). Ultraviolet–vis (UV–vis) (UV-2550 SHIMADZU, over the range of 200–2500 nm) spectrophotometer was recorded. X-ray photoelectron spectroscopy (XPS) (ESCA Lab 220i-XL electron spectrometer) analysis was conducted in a nitrogen atmosphere. The thermal conductivity of the samples in dry state was measured with Hot disk thermal constant analyzer (Hot Disk TPS2500S, Sweden) by the transient plane source method.

3. Results and discussion

3.1. Microstructure of tree root

Elm wood roots as the raw materials were sliced along vertical channel and cut into discs with a thickness of around ≈ 3 mm. The scanning electron microscopy (SEM) and micro-CT images of tree roots revealed the unique multi-level channel microstructure (Figs. 1b and 2a). The large channels are densely surrounded by narrow channels (Figs. 2b, c and S1), distributing over the entire cut surface of the tree root (Fig. 2a). Among them, the large channels are about 0.15–0.25 mm in diameter and the narrow channels are about 1.3–9.4 μm in diameter (Fig. 2d), overwhelming the channel diameter of the trunk. These multi-level channels form vertical pathways from top to bottom throughout the root segment with their diameters remaining almost constant (Fig. 2e).

The natural low-curvature channels with different hydraulic conductivities ensure the need for continuous evaporation of brine by rapidly transporting water through capillary force. The multi-level channels are meanwhile interconnected by aligned horizontal holes, namely pits, distributed through cell walls (Fig. 2f). These pits, as the main pathways for exchange of fluids and other substances between fiber tracheids or vessels, offer an imperative role in the salt equilibrium between the multi-level channels during solar desalination. Due to different hydraulic conductivities of the multi-level channels, the narrow channels with higher salt concentration could render a mass transfer to the large channels with lower salt concentration. The concentrated salt is further dissolved back without blocking the interconnect channels for a high efficacy. All these intrinsic microstructures critically enable the root-based solar evaporator with high brine transport capability and excellent anti-salt-accumulation performance.

3.2. Design and characterization of the tree-root based solar evaporator

The design and manufacturing process flow of the tree-root based solar evaporator were illustrated in Fig. 3a. Acting as the support material of solar evaporator, the hydrophilicity was designated *via* a facile

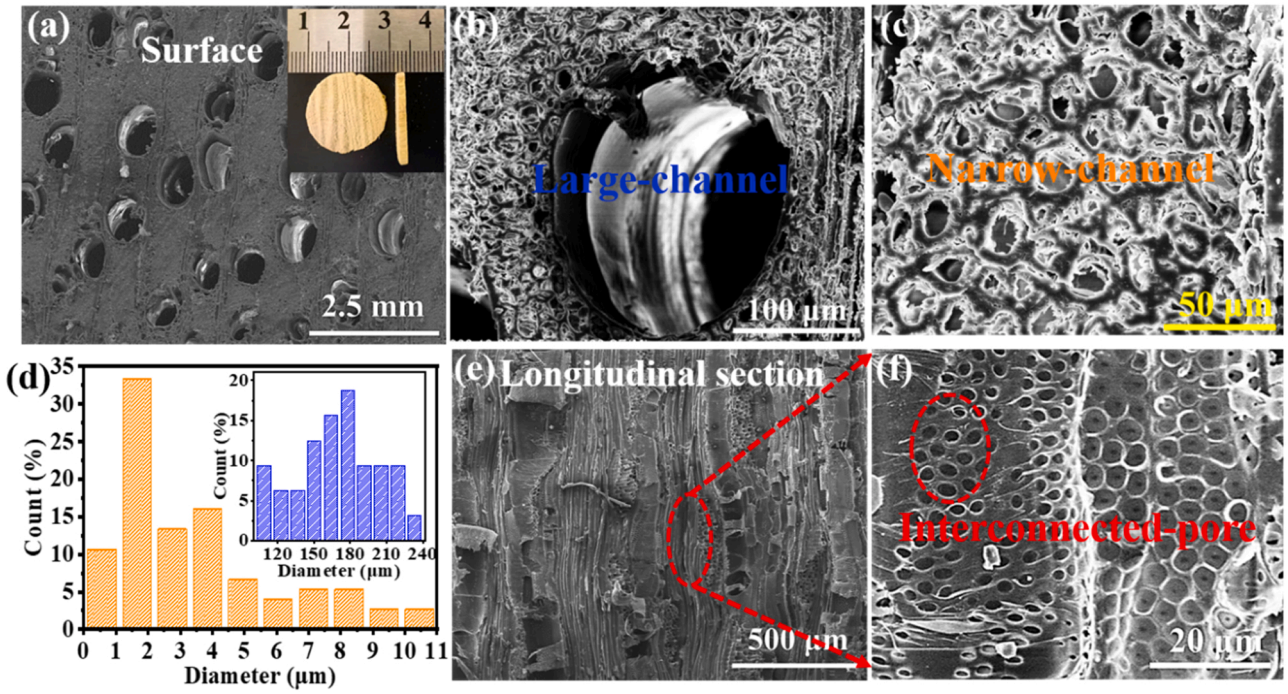

Fig. 2. Morphology characterization of the tree root. (a-c) Top-view SEM images showing the hierarchical channel structure of the evaporator. (d) Size distribution of large and small channels. (e) Side-view SEM showing structure and (f) channel-array of tree root and the interconnected-pore structures on the cell walls.

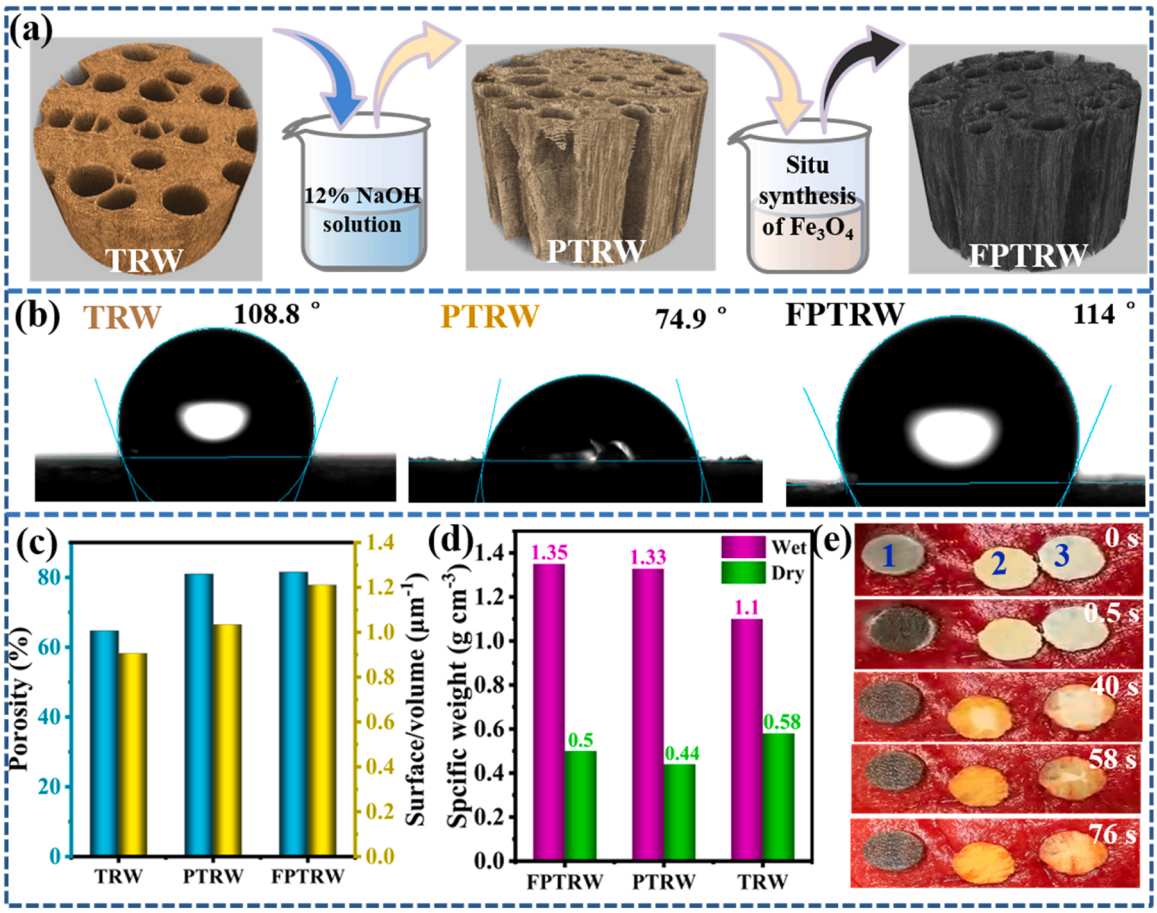

Fig. 3. (a) Schematic illustrating the transformation of tree root into photothermal materials for solar steam generation. (b) Images showing the initial water contact angle of natural tree root wood (TRW), pretreated tree root wood (PTRW), and roots loaded with Fe_3O_4 (FPTRW). The porosity (c), Specific weight change (d) of the TRW, PTRW, FPTRW, indicating their porosity. (e) Photographs showing the water flow from bottom to top surface of PTRW (coded 1), TRW (coded 2), and wood trunk (coded 3) samples respectively.

treatment using 12 wt% NaOH solution to partially remove hydrophobic native lignin (Figs. 3a-b and S2). It is noteworthy that the diameter of the internal channels remained almost unchanged after partial removal of lignin from the raw tree root (Fig. S3 a-c). However, minor part of the walls of the narrow channels were slightly damaged, benefiting inter-channel connectivity and increasing capillary force. This furthermore enhances the water transfer rate and the mass exchange capacity between the channels. Nevertheless, the top surface appears numerous nanoscale gaps and defects in the tree-root matrix, enhancing the microporous structure and porosity of raw material (Figs. 3c and S3f). Specifically, the pretreated root wood blocks (PTRW) exhibits an extreme short time window of only 0.5 s in regards to a complete transportation of Congo red solution from bottom to top surface and spreading over the upper surface, while the same process takes 48 s and 78 s for tree root wood (TRW) and trunk wood (TW), respectively (Fig. 3e). The ultra-high-speed water transportation capability of the delignified tree root is beneficial to continuously supply the water lost owing to the massive evaporation from top surface, which is also the critical factor to achieve excellent anti-salt-accumulation property of the fabricated solar desalination device.

As another core component of designing high-efficiency solar evaporator, the selection of photothermal materials is crucial (Cao et al., 2021; Kaviti et al., 2021). Considering its advantages of low-cost, strong and broadband light absorption, abundant material sources, scalability, and easy fabrication, Fe_3O_4 has been recognized as an ideal photothermal materials. Fe_3O_4 can also efficiently absorb and convert sunlight into thermal energy that heats water on the liquid/vapor interface to produce steam (Asuha et al., 2012; Dong et al., 2020; Han et al., 2021; Wu et al., 2017). The ions (Fe^{2+} and Fe^{3+}) can complex with the exposed hydroxyl groups (cellulose, hemicellulose, and lignin) on the surface of the pretreated tree root wood (PTRW), forming a good binding force (Qin et al., 2022). Hereby, Fe_3O_4 nanoparticles were *in situ* generated and deposited on the surface of PTRW as a nanocoating layer by adding ammonia to the solution (Fig. 3a).

The as-obtained treated tree root is denoted as FPTRW. The surface coated Fe_3O_4 nanoparticles changed the wettability of the FPTRW surface as indicated by initial contact angle of 114° where as PTRW exhibiting an initial contact angle of ~74.9° (Fig. 3b). The formed upper hydrophobic photothermal layer together with a bottom hydrophilic substrate has been validated as an effective way to advance the anti-salt-accumulation function, and to improve the durability of solar evaporator (Chen et al., 2020). To assess the water absorption properties, we measured the specific gravity of the prepared tree root substrates before and after water absorption. The specific gravity of wet substrates was twice than that of dried samples, demonstrating a highly porous structure of tree root with high water absorption capacity (Fig. 3d).

To verify the effect of the preparation process on the internal structure and surface morphology of the PTRW, the micro- and nano-scaled structure of fabricated tree-root based evaporator (FPTRW) was examined *via* SEM imaging. The disordered accumulation of Fe_3O_4 nanoparticles spontaneously formed mountain-shaped photothermal absorber surface with peaks and troughs (Fig. 4a-c). This undulating absorber layer greatly increases the surface area of the FPTRW evaporator, thus enhancing light absorption capability. In addition, the rough

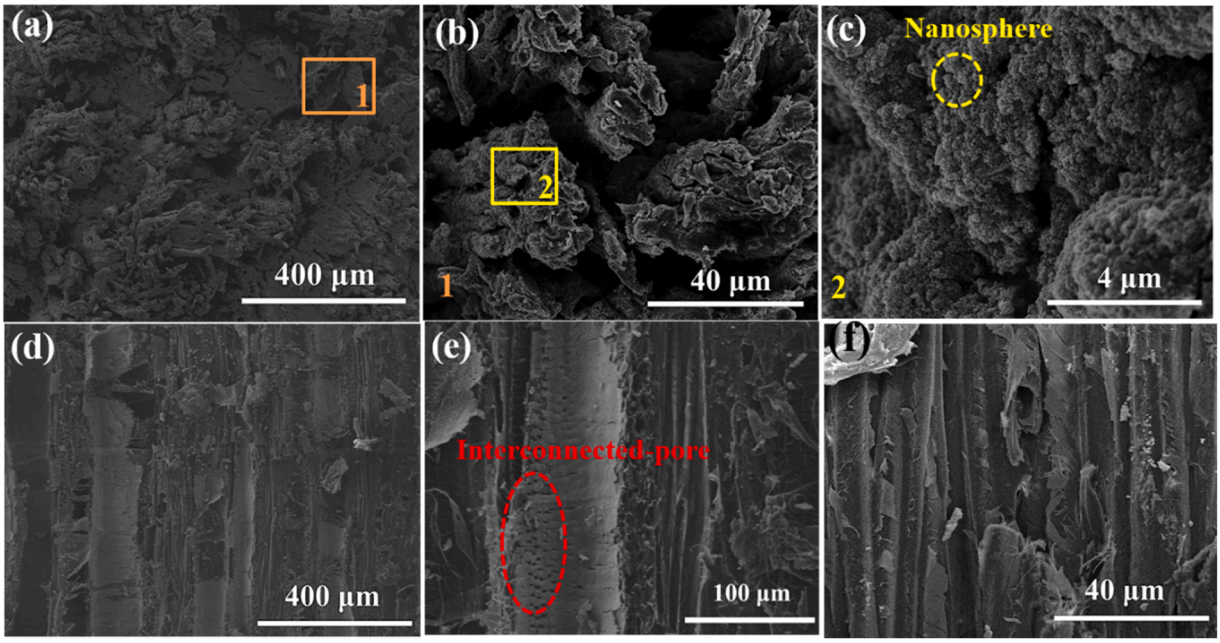

Fig. 4. Morphology characterization of the FPTRW. (a-c) SEM image of the top view showing the surface morphology and loaded nanoparticles of the evaporator. (d-f) Side-view SEM showing microstructure and channel-array of FPTRW and the interconnected pores on the cell walls.

surface of FPTRW effectively reduces the reflection of light compared to the flat surface, which could facilitate the concentration of heat and effectively reduce heat loss (Ma et al., 2021). Meanwhile, the effect of the deposition of Fe_3O_4 nanoparticles on the internal channel morphology of FPTRW was not obvious and no blockage occurred in both large and narrow channels compared with PTRW (Fig. 4d-f). The numerous pits on the cell wall were remaining interconnected between neighbouring channels, so the *in situ* synthesized nanospheres would not decrease in the water transport rate of FPTRW.

Furthermore, XPS analysis was performed to determine the elements, oxidation state, and nanoparticle binding. In contrast to the C1 spectra, after loading Fe_3O_4 nanoparticles (Fig. 5a and d), the peaks of C—C bond, C—O bond, and C═C bond on the surface of FPTRW were significantly weakened and the peak bands were shifted. This is due to the growth of nanoparticles on the surface of the FPTRW that masked the surface of the PTRW weakening of the band intensity. The iron in the generated nanoparticles interacted with the surface hydroxyl groups on the PTRW in an allotropic manner, causing the band shift (Fig. 5d). In addition, a new band appeared in the O1 spectrum of FPTRW (Fig. 5b and e), proving the successful *in situ* grown nanoparticles in the Fe oxide state. The band intensity of C and O elements in FPTRW reduced, as well as the proportion of O elements increased significantly (Fig. 5c), which also indicates that the generated nanoparticles are Fe oxide. Moreover, Fig. 5e shows the XPS spectra of the sample in the Fe 2p region with peak levels of 710.5 eV and 723.8 eV for Fe 2p 3/2 and Fe 2p 1/2, respectively, which are consistent with the f values reported in the literature for Fe_3O_4, further confirming the formation of Fe_3O_4(Yamashita and Hayes, 2008). Despite being loaded with magnetic particles, the evaporator is still light enough to float perfectly on water (Fig. S6) and has excellent stability to operate in harsh conditions (Fig. S7).

3.3. Photothermal conversion and solar desalination performance

Macroscopically, the surface of the FPTRW is visually observed to be black (Fig. S4a and b), indicating that it reflects very little light. We further explored the photothermal property of the tree-root-based evaporator, where the surface temperature of the FPTRW in air rapidly increased to 77.1 °C within 35 min under 1 sun irradiation (Fig. 5g). When it is floating in water, the absorber layer of FPTRW was rapidly heated and increased rapidly from water temperature to 37.2 °C within 40 min as indicated by infrared imaging (Fig. 5g). This resulted in a lower equilibrium temperature than air temperature due to an energy balance between the energy captured by the surface and the heat consumed by water evaporation. The heating rate of the FPTRW after loading nanoparticles was even faster than that of the delignified tree root (PTRW), and the equilibrium temperature was significantly higher than that of the PTRW at 16.6 °C (Fig. 5h). Moreover, the surface temperature of FPTRW remained constant over a long period, reflecting the evaporator's efficient energy capability to continuously deliver thermal energy for driving the heating and evaporation of water. The light absorption capacity of the tree-root-based evaporator was evaluated using a UV-NIR spectrophotometer. As shown in Fig. 5i, FPTRW with coating of Fe_3O_4 nanoparticles exhibits much higher strong light absorption, exceeding 1.5 for 200–2500 nm under the same conditions comparing with the poor light absorption of PTRW. This high absorbance ensures the excellent photothermal transformation capability of the rough mountain-shaped Fe_3O_4 layer, demonstrating its promising application in the process of highly-efficient solar evaporation.

The solar evaporation performance of the tree-root based evaporator was measured under 1 sun irradiation with a concentration of 3.5 wt% NaCl solution. For the FPTRW (Fig. 6a), an evaporation rate of 1.64 kg m^{-2} h^{-1} was achieved, which was about 5 folds higher than that of no nanoparticles loaded tree root evaporator (PTRW, 0.33 kg m^{-2} h^{-1}), confirming the key role of the mountain-shaped absorber surface. To the best of our knowledge, the evaporation rate of tree-root based FPTRW reached the efficiency plateau among all the wood-based evaporators (Table S1). More specifically, under 1 sun irradiation, the evaporation efficiency of FPTRW impressively reaches 96%, representing the highest value for all reported wood-based solar evaporator (Table S1). In addition, the water evaporation of FPTRW resulted in a high mass loss, confirming a splendid solar evaporator performance, and the high evaporation rate indicates its great potential application in practical solar water vapor power generation (Fig. 6b). This superior performance of the tree-root based evaporator can be attributed to the following aspects: (1) the nano-scaled rough mountain-shaped Fe_3O_4 nanoparticle absorber layer renders a very high surface area for highly-efficient light absorption as well as photothermal conversion; (2) the low thermal conductivity of the used tree-root substrate can effectively

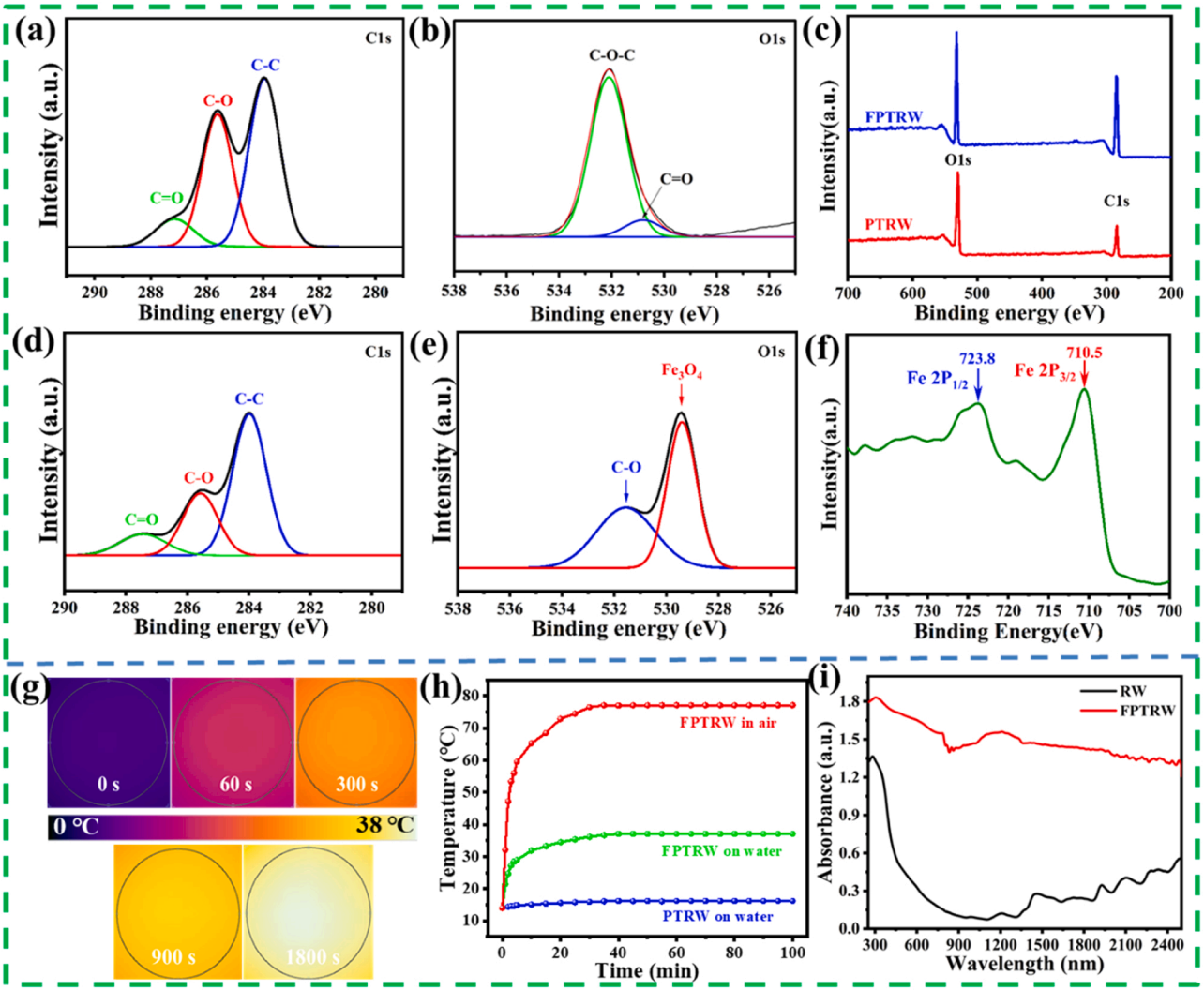

Fig. 5. (a) C1s XPS spectra of PTRW. (b) O1s XPS spectra of PTRW. (c) XPS spectra of the PTRW, FPTRW. (d) C1s XPS spectra of FPTRW. (e) O1s XPS spectra of FPTRW. (f) XPS spectra of the FPTRW. (g) IR images of the top surface for FPTRW under 1 sun irradiation. (h) The temperature changes of PTRW, FPTRW on water and FPTRW in air under 1 sun irradiation with increasing time. (i) Experimentally measured light absorption spectra for TRW and FPTRW.

reduce the heat loss (≈0.29 W m^{-1} K^{-1} for delignified tree root, Fig. S5); (3) the excellent water transport capability enables an adequate water supply for continuous evaporation on the top layer.

3.4. Salt-resistant ability of the tree-root based solar evaporator

To evaluate the stability of the solar desalination devices, we also prepared the wood trunk-based evaporator (FPTTW) under the same conditions and placed it in 3.5 wt% seawater. The fabricated tree-root based evaporator (FPTRW) exhibits excellent stable desalination process with an evaporation rate of around 1.6 kg m^{-2} h^{-1} under 1 sun illumination for 5 h (Fig. 6c). On the contrary, the evaporation rate of FPTTW was slightly lower than that of FPTRW at the beginning of the evaporator operation, while the evaporation efficiency gradually decreased after a period of evaporation (Fig. 6c). After 5 h continuous solar evaporation in 7% NaCl solution, numerous salt crystals could be observed on the top surface of the FPTTW (Fig. 6d), resulting in a significant reduction of solar energy absorption and deterioration of vapor production and further causing the decrease of evaporation rate. In contrast, no salt crystals appeared on the top evaporation layer of FPTRW, demonstrating the superior anti-salt-accumulation capability. During the desalination process using the previously reported evaporator, water evaporates rapidly at the heating interface, leading to a significant increase in local salt concentration. When the salt concentration reaches saturation, it will inevitably lead to the precipitation and accumulation of salt at the vaporization interface and gradually block the water transport path. Crucially, the fabricated tree-root based evaporator showed excellent salt-resistance, maintaining high efficiency at high salt concentrations for a long-term operation without salt precipitation on its top surface. This is mostly attributed to the vertically aligned multilevel hydrophilic channels of tree root-based substrate, connecting the top absorber interface and the bottom bulk water, which exhibits an ultra-fast water transportation and concentrated brine exchange capability. The water flux in the large diameter channels are much higher than that in the narrow diameter channels under same pressure gradient (Fig. 6e). The salt concentration in the large-diameter channels are much lower than that in the narrow-channels at the same solar irradiance, resulting in an in-plane concentration gradient. When the large-diameter channels and the narrow-diameter channels are interconnected by pits, salt exchange between the two channels occurs spontaneously, driven by the concentration gradient. Due to the fast water conduction, the increased salt in the large channel tends to diffuse rapidly backwards to the bulk water by salt exchange (Fig. 6e). For the wood-trunk based evaporator, the vertically aligned channels are relatively narrow and the concentration difference of brine in the channels is low. The effective driving force is lacking for mass exchange, thus

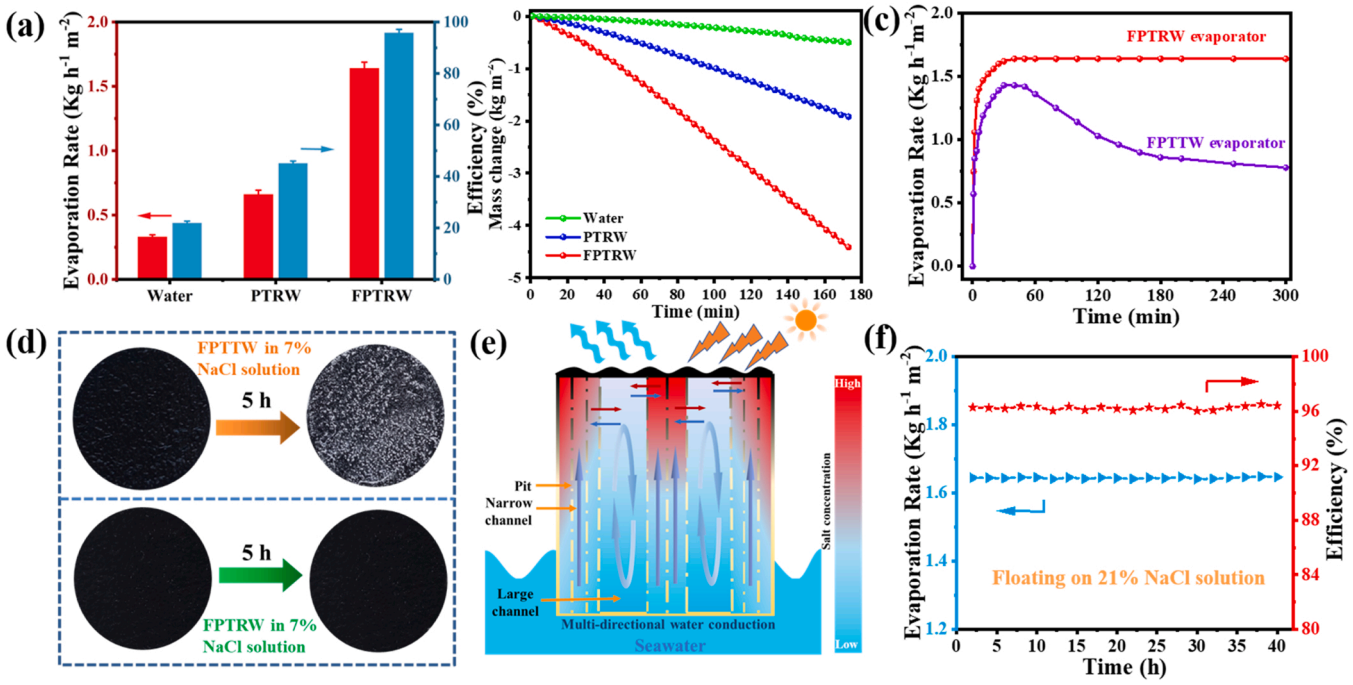

Fig. 6. (a) Evaporation rate and efficiency of water of FPTRW, PTRW and sea water under 1 sun irradiation (1 kW m^{-2}). (b) Mass loss of water of FPTRW, PTRW and sea water under 1 sun irradiation. (c) Evaporation rates of FPTRW and the wood trunk-based evaporator (FPTTW) for continuous 300 min desalination in seawater. (d) Surface pictures of FPTRW and FPTTW after 300 min of desalination. (e) Schematic diagram illustrating the salt resistance mechanism of the FPTRW evaporator (f) Duration test of the FPTRW based on continuous solar desalination for 40 h on 21% NaCl solution under 1 sun irradiation.

leading to the severe salt accumulation. Therefore, with this multi-directional mass transfer mechanism, our tree-root based evaporator achieves real-time salt-rejecting ability and exhibits long-term stability, without salt precipitation even in a 21 wt% NaCl solution with 40 h of continuous solar evaporation under 1 sun irradiation (Figs. 6f and S8). In addition, compared with other solar evaporator fabricated using synthetic materials, the solar evaporation device using natural tree roots is low cost due to the abundant and renewable forest resource and lack of effective utilization of tree roots, which makes it unparalleled potential for practical application in seawater desalination.

4. Conclusion

In summary, tree roots with intrinsic hierarchically multi-scale channels and interconnected porous microstructures serve as a promising candidate for solar evaporator base. For the first time, the tree-root based solar evaporator was fabricated *via* a bilayer structure design with different wetting properties. Current design exhibits a superior anti-salt-accumulation with stable and highly-efficient solar desalination capability even in 21% brine under 1 sun irradiation. The unique super-hydrophilic tree root substrate with excellent mass exchange and ultra-high-speed water transport capability play a vital role in efficient and continuous solar desalination. The interconnected multi-scale channels by the numerous pits drive salt exchange through concentration differences. Together with the hydrophobic top surface, the design provides salt resistance stability for the evaporator. A mountain-shaped hydrophobic absorber surface obtained from the *in situ* synthesized Fe_3O_4 nanoparticles increases the surface area and surface roughness on nano-dimension, exhibiting extensive and strong light absorption as the photothermal absorption layer. With these unique architectures, the tree root-based solar evaporator imparts an evaporation rate of 1.64 kg m^{-2} h^{-1} and conversion efficiency of 96% under 1 sun irradiation, representing the highest value for all reported wood-based solar evaporator. This tree root evaporator provides a highly-efficient, low-cost, environmentally friendly, long-term stable solar desalination strategy, showing to be a promising substrate for solar water purification, water management, and pollution reduction. Expanding the functional applications of tree roots is expected to bring greater value to forestry residuals raising up techno-economic value and natural sustainability. Moreover, this work also inspires material scientist to explore a bottom-up approach for designing evaporators mimicking natural root structure.

Declaration of Competing Interest

The authors declare that they have no known competing financial interests or personal relationships that could have appeared to influence the work reported in this paper.

Data availability

Data will be made available on request.

Acknowledgements

The project was supported by the National Natural Science Foundation of China (No. 32001269 and No. 31870563) and the QUTJBZ Program (No. 2022JBZ01–05).

Appendix A. Supporting information

Supplementary data associated with this article can be found in the online version at doi:10.1016/j.indcrop.2023.116507.

References

Asuha, S., Wan, H.L., Zhao, S., Deligeer, W., Wu, H.Y., Song, L., Tegus, O., 2012. Water-soluble, mesoporous Fe3O4: Synthesis, characterization, and properties. Ceram. Int. 38, 6579–6584.

Bian, Y., Tang, K., Tian, L.Y., Zhao, L.J., Zhu, S.M., Lu, H., Yang, Y., Ye, J.D., Gu, S.L., 2021. Sustainable solar evaporation while salt accumulation. Acs Appl. Mater. Inter 13, 4935–4942.

Cao, S., Rathi, P., Wu, X., Ghim, D., Jun, Y.S., Singamaneni, S., 2021. Cellulose nanomaterials in interfacial evaporators for desalination: A “natural” choice. Adv. Mater. 33, 2000922.
Chen, C., Li, Y., Song, J., Yang, Z., Kuang, Y., Hitz, E., Jia, C., Gong, A., Jiang, F., Zhu, J., 2017. Highly flexible and efficient solar steam generation device. Adv. Mater. 29, 1701756.
Chen, C.J., Kuang, Y.D., Hu, L.B., 2019. Challenges and opportunities for solar evaporation. Joule 3, 683–718.
Chen, J., Yin, J.L., Li, B., Ye, Z., Liu, D., Ding, D., Qian, F., Myung, N.V., Zhang, Q., Yin, Y., 2020. Janus evaporators with self-recovering hydrophobicity for salt-rejecting interfacial solar desalination. ACS Nano.
Djellabi, R., Noureen, L., Dao, V., Meroni, D., Falletta, E., Dionysiou, D.D.D., Bianchi, C. L., 2022. Recent advances and challenges of emerging solar-driven steam and the contribution of photocatalytic effect. Chem. Eng. J. 431.
Dong, X., Cao, L., Si, Y., Ding, B., Deng, H., 2020. Cellular Structured CNTs@SiO2 Nanofibrous Aerogels with Vertically Aligned Vessels for Salt-Resistant Solar Desalination. Adv. Mater. 32, e1908269.
Elimelech, M., Phillip William, A., 2011. The future of seawater desalination: energy, technology, and the environment. Science 333, 712–717.
Hafner, B.D., Hesse, B.D., Bauerle, T.L., Grams, T.E.E., 2020. Water potential gradient, root conduit size and root xylem hydraulic conductivity determine the extent of hydraulic redistribution in temperate trees. Funct. Ecol. 34, 561–574.
Han, X., Besteiro, L.V., Koh, C.S.L., Lee, H.K., Phang, I.Y., Phan-Quang, G.C., Ng, J.Y., Sim, H.Y.F., Lay, C.L., Govorov, A., Ling, X.Y., 2021. Intensifying Heat Using MOF-Isolated Graphene for Solar-Driven Seawater Desalination at 98% Solar-to-Thermal Efficiency. Adv. Funct. Mater. 31.
He, S., Chen, C., Kuang, Y., Mi, R., Liu, Y., Pei, Y., Kong, W., Gan, W., Xie, H., Hitz, E., 2019. Nature-inspired salt resistant bimodal porous solar evaporator for efficient and stable water desalination. Energ. Environ. Sci. 12, 1558–1567.
Jia, C., Li, Y., Yang, Z., Chen, G., Yao, Y., Jiang, F., Kuang, Y., Pastel, G., Xie, H., Yang, B., 2017. Rich mesostructures derived from natural woods for solar steam generation. Joule 1, 588–599.
Jiang, Q., Derami, Gholami, Ghim, H., Cao, D., Jun, S., Singamaneni, S, Y.-S., 2017. Polydopamine-filled bacterial nanocellulose as a biodegradable interfacial photothermal evaporator for highly efficient solar steam generation. J. Mater. Chem. A 5, 18397–18402.
Kaviti, A.K., Sri Ganesh Balaji, J., Siva Ram, A., Aruna Kumari, A., 2021. An overview on hydrogel materials for solar desalination. Mater. Today.: Proc. 44, 2526–2532.
Kuang, Y.D., Chen, C.J., He, S.M., Hitz, E.M., Wang, Y.L., Gan, W.T., Mi, R.Y., Hu, L.B., 2019. A high-performance self-regenerating solar evaporator for continuous water desalination. Adv. Mater. 31.
Kumar, R., Raizada, P., Verma, N., Hosseini-Bandegharaei, A., Thakur, V.K., Le, Q.V., Nguyen, V.-H., Selvasembian, R., Singh, P., 2021. Recent advances on water disinfection using bismuth based modified photocatalysts: Strategies and challenges. J. Clean. Prod. 297, 126617.
Kummu, M., Guillaume, J.H.A., de Moel, H., Eisner, S., Flörke, M., Porkka, M., Siebert, S., Veldkamp, T.I.E., Ward, P.J., 2016. The world’s road to water scarcity: shortage and stress in the 20th century and pathways towards sustainability. Sci. Rep. 6.
Li, F., Li, N., Wang, S., Qiao, L., Yu, L., Murto, P., Xu, X., 2021. Self-repairing and damage-tolerant hydrogels for efficient solar-powered water purification and desalination. Adv. Funct. Mater. 31, 2104464.
Li, N., Qiao, L., He, J., Wang, S., Yu, L., Murto, P., Li, X., Xu, X., 2020. Solar-driven interfacial evaporation and self-powered water wave detection based on an all-cellulose monolithic design. Adv. Funct. Mater. 31.
Li, T., Liu, H., Zhao, X., Chen, G., Dai, J., Pastel, G., Jia, C., Chen, C., Hitz, E., Siddhartha, D., 2018. Scalable and highly efficient mesoporous wood-based solar steam generation device: localized heat, rapid water transport. Adv. Funct. Mater. 28, 1707134.
Li, Z., Wang, C., Lei, T., Ma, H., Su, J., Ling, S., Wang, W., 2019. Arched bamboo charcoal as interfacial solar steam generation integrative device with enhanced water purification capacity. Adv. Sustain. Syst. 3, 1800144.
Ma, C., Liu, Q., Peng, Q., Yang, G., Jiang, M., Zong, L., Zhang, J., 2021. Biomimetic hybridization of janus-like graphene oxide into hierarchical porous hydrogels for improved mechanical properties and efficient solar desalination devices. ACS Nano 15, 19877–19887.
McElrone, A.J., Pockman, W.T., Martínez-Vilalta, J., Jackson, R.B., 2004. Variation in xylem structure and function in stems and roots of trees to 20 m depth. N. Phytol. 163, 507–517.
Qin, J., Li, N., Jiang, M., Zong, L., Yang, H., Yuan, Y., Zhang, J., 2022. Ultrasonication pretreatment assisted rapid co-assembly of cellulose nanocrystal and metal ion for multifunctional application. Carbohydr. Polym. 277.
Sharshir, S.W., Kandeal, A.W., Ellakany, Y.M., Maher, I., Khalil, A., Swidan, A., Abdelaziz, G.B., Koheil, H., Rashad, M., 2022. Improving the performance of tubular solar still integrated with drilled carbonized wood and carbon black thin film evaporation. Sol. Energy 233, 504–514.
Shi, Z., Zhou, D., Wu, Y., Pan, G., Xu, W., Wang, N., Liu, S., Sun, R., Liu, L., Zhuang, X., Zhang, Y., Lu, S., Song, H., 2022. Dual interfacial engineering to improve ultraviolet and near-infrared light harvesting for efficient and stable perovskite solar cells. Chem. Eng. J. 435, 134792.
Storer, D.P., Phelps, J.L., Wu, X., Owens, G., Khan, N.I., Xu, H., 2020. Graphene and Rice-Straw-Fiber-Based 3D Photothermal Aerogels for Highly Efficient Solar Evaporation. ACS Appl. Mater. Interfaces 12, 15279–15287.
Tao, P., Ni, G., Song, C., Shang, W., Wu, J., Zhu, J., Chen, G., Deng, T., 2018. Solar-driven interfacial evaporation. Nat. Energy 3, 1031–1041.
Tian, Y., Deng, P., Wu, Y., Li, J., Liu, J., Li, G., He, Q., 2020. MnO2 Nanowires-Decorated Reduced Graphene Oxide Modified Glassy Carbon Electrode for Sensitive Determination of Bisphenol A. J. Electrochem. Soc. 167.
Wang, C., Wang, J., Li, Z., Xu, K., Lei, T., Wang, W., 2020. Superhydrophilic porous carbon foam as a self-desalting monolithic solar steam generation device with high energy efficiency. J. Mater. Chem. A 8, 9528–9535.
Wang, Y., Liu, H., Chen, C., Kuang, Y., Song, J., Xie, H., Jia, C., Kronthal, S., Xu, X., He, S., 2019. All natural, high efficient groundwater extraction via solar steam/vapor generation. Adv. Sustain Syst. 3, 1800055.
Wang, Y., Wu, X., Wu, P., Zhao, J., Yang, X., Owens, G., Xu, H., 2021. Enhancing solar steam generation using a highly thermally conductive evaporator support. Sci. Bull. 66, 2479–2488.
Wei, C., Zhang, X., Ma, S., Zhang, C., Li, Y., Chen, D., Jiang, H., Xu, Z., Huang, X., 2021. Ultra-robust vertically aligned three-dimensional (3D) Janus hollow fiber membranes for interfacial solar-driven steam generation with salt-resistant and multi-media purification. Chem. Eng. J. 425.
Wu, X., Chen, G.Y., Zhang, W., Liu, X., Xu, H., 2017. A plant-transpiration-process-inspired strategy for highly efficient solar evaporation. Adv. Sustain. Syst. 1, 1700046.
Xu, K., Wang, C., Li, Z., Wu, S., Wang, J., 2021. Salt mitigation strategies of solar-driven interfacial desalination. Adv. Funct. Mater. 31, 2007855.
Xu, Z.R., Li, Z.D., Jiang, Y.H., Xu, G.X., Zhu, M.W., Law, W.C., Yong, K.T., Wang, Y.S., Yang, C.B., Dong, B.Q., Xing, F., 2020. Recent advances in solar-driven evaporation systems. J. Mater. Chem. A 8, 25571–25600.
Xue, G., Liu, K., Chen, Q., Yang, P., Li, J., Ding, T., Duan, J., Qi, B., Zhou, J., 2017. Robust and low-cost flame-treated wood for high-performance solar steam generation. Acs Appl. Mater. Inter 9, 15052–15057.
Yamashita, T., Hayes, P., 2008. Analysis of XPS spectra of Fe2+ and Fe3+ ions in oxide materials. Appl. Surf. Sci. 254, 2441–2449.
Zang, L.L., Finnerty, C., Zheng, S.X., Conway, K., Sun, L.G., Ma, J., Mi, B.X., 2021. Interfacial solar vapor generation for desalination and brine treatment: Evaluating current strategies of solving scaling. Water Res 198.
Zhang, Y.X., Xiong, T., Nandakumar, D.K., Tan, S.C., 2020. Structure architecting for salt-rejecting solar interfacial desalination to achieve high-performance evaporation with in situ energy generation. Adv. Sci. 7.
Zhao, F., Guo, Y., Zhou, X., Shi, W., Yu, G., 2020. Materials for solar-powered water evaporation. Nature Reviews. Materials 5, 388–401.
Zhou, X., Guo, Y., Zhao, F., Yu, G., 2019. Hydrogels as an emerging material platform for solar water purification. Acc. Chem. Res. 52, 3244–3253.
Zhu, L., Gao, M., Peh, C.K.N., Ho, G.W., 2019. Recent progress in solar-driven interfacial water evaporation: Advanced designs and applications. Nano Energy 57, 507–518.
Zhu, M.W., Li, Y.J., Chen, F.J., Zhu, X.Y., Dai, J.Q., Li, Y.F., Yang, Z., Yan, X.J., Song, J. W., Wang, Y.B., Hitz, E., Luo, W., Lu, M.H., Yang, B., Hu, L.B., 2018. Plasmonic wood for high-efficiency solar steam generation. Adv. Energy Mater. 8.